



OPEN ACCESS

EDITED BY

Yubing Liu,
China University of Mining and
Technology, China

REVIEWED BY

Xuelong Li,
Shandong University of Science and
Technology, China
Wenpu Li,
Taiyuan University of Technology, China

*CORRESPONDENCE

Chongyang Wang,
✉ wcy@cqu.edu.cn
Dongming Zhang,
✉ Zhangdm@cqu.edu.cn

RECEIVED 23 May 2023

ACCEPTED 23 June 2023

PUBLISHED 03 July 2023

CITATION

Li S, Wang C, Zhang D, Wang M, Zhou F
and Pan Y (2023), Deterioration
mechanism of mechanical properties of
phosphorite under different
saturation duration.
Front. Earth Sci. 11:1227742.
doi: 10.3389/feart.2023.1227742

COPYRIGHT

© 2023 Li, Wang, Zhang, Wang, Zhou and
Pan. This is an open-access article
distributed under the terms of the
[Creative Commons Attribution License
\(CC BY\)](https://creativecommons.org/licenses/by/4.0/). The use, distribution or
reproduction in other forums is
permitted, provided the original author(s)
and the copyright owner(s) are credited
and that the original publication in this
journal is cited, in accordance with
accepted academic practice. No use,
distribution or reproduction is permitted
which does not comply with these terms.

Deterioration mechanism of mechanical properties of phosphorite under different saturation duration

Shujian Li¹, Chongyang Wang^{2,3*}, Dongming Zhang^{2,3*},
Menglai Wang¹, Fan Zhou¹ and Yisha Pan⁴

¹Yunnan Phosphate Chemical Group Co Ltd, Yunnan, China, ²State Key Laboratory of Coal Mine Disaster Dynamics and Control, Chongqing University, Chongqing, China, ³School of Resources and Safety Engineering, Chongqing University, Chongqing, China, ⁴School of Surveying, Mapping and Land Information Engineering, Henan Polytechnic University, Jiaozuo, Henan, China

In order to explore the deterioration mechanism of mechanical properties of phosphate rock under different saturation time, the degradation mechanism of phosphoric rock samples under different saturation duration was analyzed by laboratory test, theoretical analysis and neural network modeling, and the results is as follows: saturation of water will result in deterioration of mechanical properties of samples. The peak compressive strength and peak strain of the samples decreased gradually with the increase of saturation time. The average peak strength of 12, 24, and 36 h saturated specimens is 8.6%, 21.1%, and 32.2% lower than that of natural specimens, and the peak strain is 5.9%, 13.9%, and 31.3% lower, respectively. The stress-strain curves of the samples with water saturation for 36 h have more jitter stages after the peak, indicating that the plastic characteristics of the samples will be increased with water saturation for a long time. The neural network method was used to analyze the test parameters and the mechanical parameters of the samples, and the mechanical properties under the action of saturated water and confining pressure were obtained. The neural network model was established to represent the mechanical properties of the samples, and the average accuracy of the model was 0.89. The model can be used to predict and verify the mechanical properties of samples under other saturation and confining pressure conditions in the limited region. The research results can provide theoretical reference for the deterioration mechanism of confining pressure in water-rich roadway.

KEYWORDS

phosphorite, saturation duration, mechanical property, triaxial compression test, neural network

1 Introduction

The phenomenon of water gushing often occurs in the process of roadway excavation in a mine in Yunnan Province. Soaking and saturation will result in deterioration of mechanical properties of rock mass, thus increasing the difficulty of tunneling and support (Liu et al., 2023a; Liu et al., 2023b; Liu et al., 2023c). Therefore, it is of great significance to explore the deterioration mechanism of rock mechanical properties under different saturation duration conditions.

Many scholars at home and abroad have done a lot of research on the water deterioration mechanism of rock (Ni et al., 2005; Wood, 2015; Ma et al., 2020; Wang et al., 2020; Wang et al., 2023a; Wang et al., 2023b). Feng et al. (2022) explored the instability fracture

characteristics of red sandstone samples under different water-bearing states under the combination of static and dynamic states through laboratory tests, and concluded that the mechanical response of natural sandstone samples was typical characteristic of rock burst, while the mechanical response of saturated sandstone samples was mainly reflected in the degree of rock sample fragmentation. In the study on the changes of rock mechanical properties and meso-structural characteristics under water saturation, Zhao (2022) conducted triaxial compression and scanning electron microscope tests under different confining pressures and water saturation conditions, and concluded that with the increase of water saturation, the mechanical properties of sandstone continue to decline, the water saturation deterioration effect of sandstone is significant, and the water saturation effect promotes the development of microcracks. Water and rock sample volume have obvious influences on physical mechanics and deformation characteristics of sandstone. Through experiments, Wang et al. (2019) concluded that: the elastic modulus and deformation modulus of sandstones are negatively correlated with the rock sample volume. The Poisson's ratio of dry sandstones increases with the increase of rock sample volume, while that of saturated sandstones increases first with the increase of rock sample volume and then becomes stable. The presence of water has no obvious effect on the failure morphology of rock sample under uniaxial compression. In the study on deformation characteristics of saturated rock mass in cold region, Jia et al. (2023) pointed out that the freeze-thaw strain characteristic values of saturated rock are related to fracture length, width and rock lithology, and that freeze-thaw failure of fractured rock is a process of gradual accumulation of residual strain. Water environments (water content, osmotic water pressure), loading rates, generalized stress relaxation have obvious deterioration effects on the aging characteristics of rock. Considering the aging characteristics of surrounding rock under the action of water environment, it is of great significance for the long-term stability control of tunnel (Chen, 2021). By studying the tensile strength and failure mechanism of rock damaged by hydrothermal coupling at different loading rates, Wang et al. (2020) pointed out that the indirect tensile strength of water-saturated sandstone specimens was lower than that of dry specimens, and the strain rate dependence of water-saturated rock samples was stronger than that of dry rock. A large number of electromagnetic radiation (EMR) signals are released in the loading failure process of water-bearing fractured rock mass, which can provide certain guidance for the monitoring and warning of related geological disasters. Related research results showed that compared with dry rock samples, saturated rock samples had lower compressive strength, earlier cracking time, more complex failure mode, and lower proportion of high frequency signal of saturated rock samples than dry rock samples (Shen et al., 2021).

In recent years, neural network model has been widely used in rock mechanics research experiments (Zhang et al., 1991). Chen (2022) proposed an acoustic emission positioning method that combines spectrum analysis and convolutional neural network without the need for wave velocity model and time pick, which effectively improves the acoustic emission positioning accuracy and avoids the shortcomings of traditional positioning methods, providing a new idea for rock acoustic emission positioning. By

introducing BP neural network, Chen (2022) took drilling experiment data import as the input layer and rock mechanics parameters as the output layer. Through the prediction of composite samples, the prediction accuracy of the trained BP neural network model on rock mechanics parameters and the identification ability of rock interface were verified. By establishing the fracture network topography prediction model based on artificial neural network under the influence of multiple factors, Feng (2021) sorted the factors affecting the results of shale fracture network topography, providing a new idea to solve the environmental problems in shale gas exploitation.

The above scholars have done a lot of research on the water-bearing deterioration mechanism of rocks and reached a lot of conclusions, but there are few studies on the deterioration law of rock mechanical properties under different water-saturation duration (Zhang et al., 2018; Wu et al., 2021). Therefore, triaxial compression test were carried out on phosphate rock in this paper to explore the changes of mechanical properties of rock under three conditions of 12, 24 and 36 h. On this basis, the neural network method was used to analyze the test parameters and sample mechanical parameters. The discrete data points were extended to the continuous definition domain on the number line, and the neural network model based on multi-layer perceptron was established, in order to provide theoretical reference for the excavation and support of water-rich roadway in a Yunnan mine.

2 Sample and methods

2.1 Specimen preparation

The rock sample in this paper is taken from the phosphorus block rock in the upper layer of phosphate mine roadway in Yunnan. The selected rock sample was cut and polished to make a standard cylindrical sample with $\phi 50 \times 100$ mm. Meanwhile, in order to avoid the influence of the end friction effect on the test, the flatness of the end face was controlled within 0.02 mm, the surface of the specimen was smooth without obvious joints and cracks, and the cylindrical specimen was manufactured in strict accordance with the standards of the International Society of Rock Mechanics, as shown in Figure 1.

2.2 Testing device

1) Ultrasound Testing Device.

The longitudinal wave velocity was carried out by the UTA-2000A intelligent ultra-sonic monitor (as shown in Figure 2A). The sampling frequency is 10 MHz; sensor frequency is 35 kHz, and Vaseline cream as coupling agent is used between the sample and sensors.

2) Fatigue loading test and triaxial compression test were carried out on a QKX-YD-1000 electro-hydraulic servo rock dynamic fatigue test machine, which was produced by Qingdao Qiankunxing Intelligent Technology Co., Ltd., Qingdao, Shandong Province. As shown in Figures 2B, C. The maximum axial load of the system is 800 kN, the maximum loading speed is 800 mm/min, and the maximum displacement is 50 mm (Wang 2021).

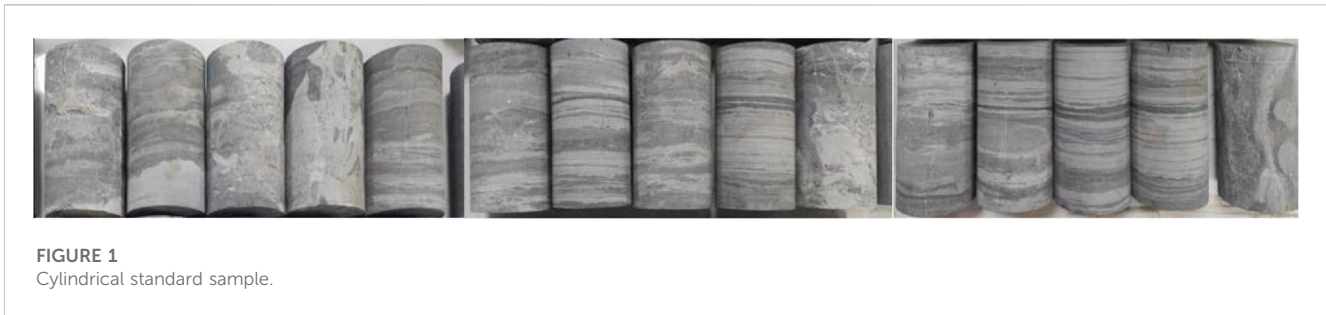


FIGURE 1
Cylindrical standard sample.

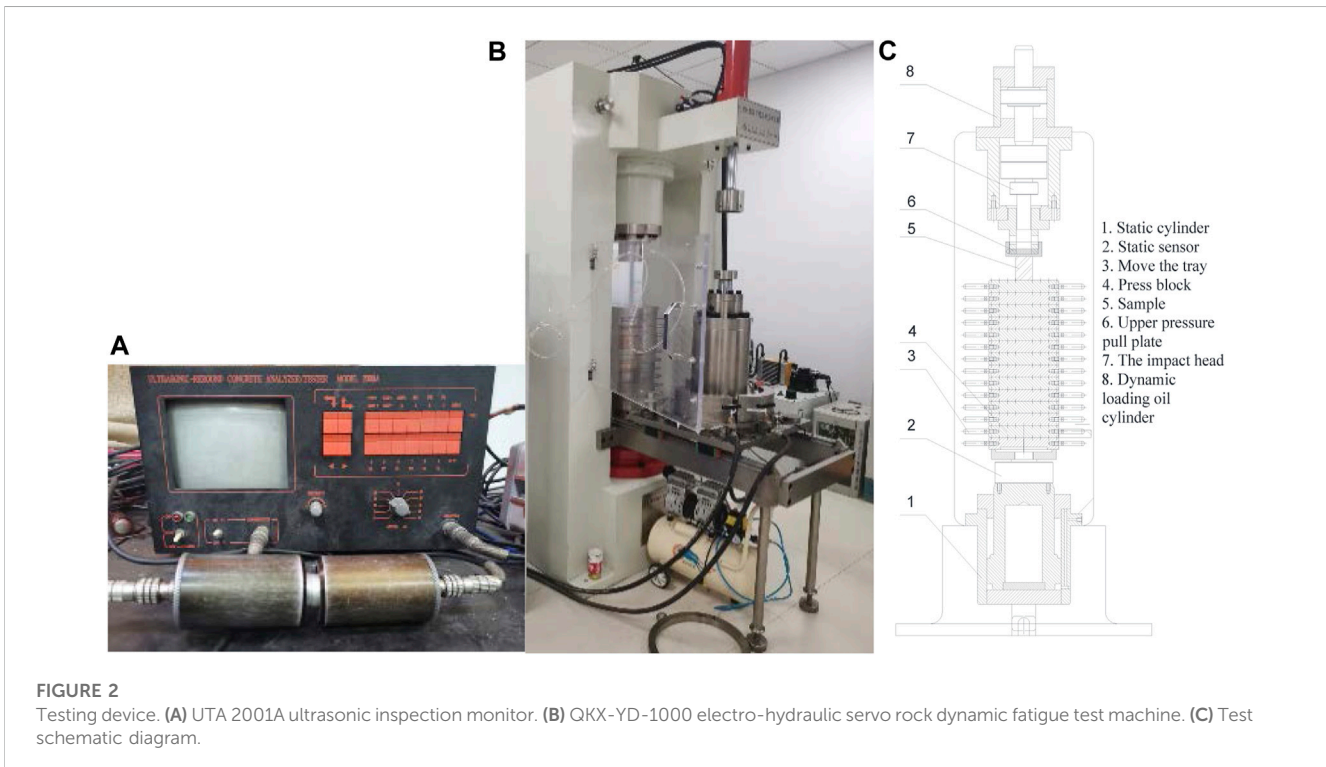


FIGURE 2
Testing device. (A) UTA 2001A ultrasonic inspection monitor. (B) QKX-YD-1000 electro-hydraulic servo rock dynamic fatigue test machine. (C) Test schematic diagram.

2.3 Test methods

- 1) Grouping: The specimens are divided into 4 groups, labeled as Group A, Group B, Group C, and Group D, with 8 specimens in each group. Group A specimens undergo no treatment and are labeled as the natural group. Specimens in Group B, Group C, and Group D were forced to fill with water in a vacuum saturator for 12, 24, 36 h, respectively, and then sealed with plastic wrap.
- 2) Measurement of physical properties: Calipers and an electronic balance are used to measure the dimensions and mass of the specimens, and calculate the density. The UTA-2000A Intelligent Ultrasonic Monitoring Instrument (Figure 3A) is used to conduct ultrasonic testing on the specimens. Based on the density and ultrasonic testing results, homogeneous specimens are selected for further testing.
- 3) Conventional triaxial tests: Conduct conventional triaxial tests on the A, B, C, and D groups of specimens to measure mechanical parameters such as peak strength (σ_1), peak strain (ϵ_c), elastic modulus (E), cohesion (c), and angle of

internal friction (f). In this experiment, the confining pressure for the three groups of specimens is set at 4, 6, 8, 10, and 12 MPa.

3 Test results and analysis

Figure 3 shows the stress-strain curves of the samples in the conventional triaxial compression test. As can be seen from Figure 3, the variation of stress-strain curve of samples of each group roughly went through four stages: compaction, elasticity, yield and failure. 1) Compaction stage: the original cracks inside the sample were compacted to form nonlinear compression deformation; 2) Elastic stage: the stress-strain curve was basically linear, obeying Hooke's law; 3) Yield stage: as the axial stress continues to load, the material with low strength inside the sample first enters the yield failure stage, the stress-strain curve deviated from the straight line, and the increased rate of axial stress gradually decreases; 4) Failure stage: when the sample reached the ultimate strength, the bearing

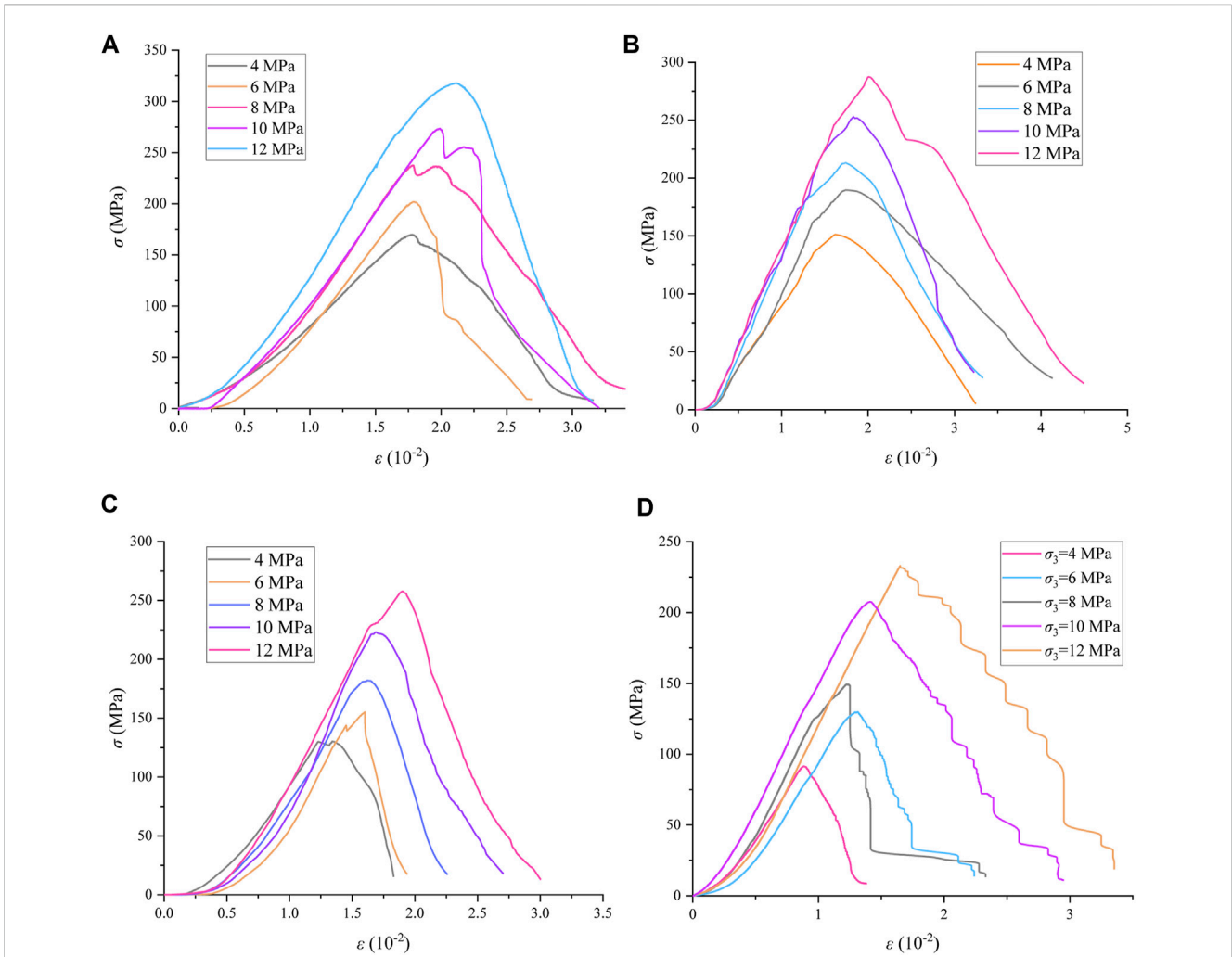


FIGURE 3 The stress-strain curves of the samples in the conventional triaxial compression test under different water length conditions. (A) Group A (0 h). (B) Group B (12 h). (C) Group C (24 h). (D) Group D (36 h).

capacity of the sample decreased rapidly with the increase of deformation, and the deformation damage of the sample was further aggravated.

Observe the peak stress of samples in each group in Figure 3. For Group A, the peak strength of the sample is 169.9 MPa when the confining pressure is 4 MPa. When the confining pressure is 6, 8, 10 and 12 MPa, the peak strength of each sample increases by 18.7%, 38.1%, 60.9%, and 87.1%, respectively. For Group B, the peak strength of the samples is 151.2 MPa when the confining pressure is 4 MPa. When the confining pressure is 6, 8, 10 and 12 MPa, the peak strength of each sample increases by 25.4%, 41.1%, 67.0%, and 90.0%, respectively. For Group C, the peak strength of the samples is 84.17 MPa when the confining pressure is 4 MPa. When the confining pressure is 6, 8, 10 and 12 MPa, the peak strength of each sample increases by 17.6%, 39.7%, 70.1%, and 97.8%, respectively. For Group D, the peak strength of the samples is 91.5 MPa when the confining pressure is 4 MPa. When the confining pressure is 6, 8, 10 and 12 MPa, the peak strength of each sample increases by 41.9%, 63.3%, 127.0%, and 154.7%, respectively.

Meanwhile, the transverse comparison of samples of each group shows that the peak strength of samples in Group A (239.5 MPa) is the largest, and the average peak strength of samples in Group B (218.8 MPa), Group C (189.1 MPa), and Group D (162.3 MPa) under different confining pressures is 8.6%, 21.1%, and 32.2% lower than that of Group A, respectively. The peak strain of samples in Group A (1.89×10^{-2}) is the largest, and the average peak strain of samples in Group B (1.78×10^{-2}), Group C (1.63×10^{-2}), and Group D (1.30×10^{-2}) under different confining pressures is 5.9%, 13.9%, and 31.3% lower than that of Group A, respectively, indicating that saturation of water has an obvious deterioration effect on samples.

According to Mohr-Coulomb strength criterion, the maximum shear stress of the sample bearing is determined by cohesion and internal friction Angle, which can be expressed as (Wei et al., 2020):

$$\tau = c + \mu\sigma \tag{1}$$

where, c is cohesion; μ is the internal friction coefficient, $\mu = \tan \varphi$, φ is the Angle of internal friction; σ is the normal stress on the surface of the damage. If expressed as principal stress, then:

TABLE 1 Mechanical parameters of each group of samples.

Group	σ_3 (MPa)	σ_1 (MPa)	ϵ_c (10^{-2})	E (GPa)	c (MPa)	φ ($^\circ$)
A (Nature)	4	169.88	1.77	12.96	10.77	63.75
	6	201.69	1.79	19.51		
	8	234.54	1.78	16.85		
	10	273.40	1.99	17.99		
	12	317.84	2.12	22.29		
B (Soak for 12 h)	4	151.24	1.62	10.88	10.35	62.58
	6	189.73	1.71	14.41		
	8	213.35	1.72	15.12		
	10	252.54	1.83	17.59		
	12	287.37	2.01	16.03		
C (Soak for 24 h)	4	130.34	1.34	18.28	7.42	62.09
	6	153.25	1.57	23.40		
	8	182.08	1.62	22.76		
	10	221.74	1.72	28.06		
	12	257.84	1.89	23.16		
D (Soak for 36 h)	4	91.49	0.88	9.51	9.00	53.13
	6	129.86	1.31	17.16		
	8	149.40	1.24	14.04		
	10	207.65	1.41	16.95		
	12	233.02	1.65	15.52		

$$\sigma_1 = k\sigma_3 + Q \tag{2}$$

where, σ_1 is the peak strength; k and Q are material strength parameters, and the relationship between their values and c , φ is as follows:

$$\varphi = \arcsin \frac{(k - 1)}{(k + 1)} \tag{3}$$

$$c = Q \frac{(1 - \sin \varphi)}{(2 \cos \varphi)} \tag{4}$$

According to Eq. 2, the relationship between the peak strength and confining pressure of the samples was obtained by regression, and the mechanical parameters of the samples of each group were calculated, as shown in Table 1.

4 Neural network analysis

4.1 Neural network model training

A neural network prediction model with saturation time and confining pressure as influencing factors was developed. In the model, peak strains, peak strength and elastic modulus as the output factors, as shown in Figure 4.

As shown in Figure 4, the activation function of the hidden layer of the multi-layer perceptron is the hyperbolic tangent function (Aras et al., 2020; Moussas et al., 2021):

$$\tanh x = \frac{\sinh x}{\cosh x} = \frac{e^x - e^{-x}}{e^x + e^{-x}} \tag{5}$$

In Figure 3, the calculation formula of the weight of each input layer is as follows:

$$\begin{cases} \omega_{1n} (1 \times 3) = [\text{random} (-1, 1) \times 3] \\ \omega_{2n} (1 \times 4) = [\text{random} (-1, 1) \times 4] \end{cases} \tag{6}$$

- 1) Set the initial random weight (for the convenience of calculation, we take the deviation as the first input factor), where $\omega_{1n} (1 \times 3)$ and $\omega_{2n} (1 \times 4)$ are the weights of the input layer and the hidden layer, respectively.
- 2) The factors of the input layer are multiplied by the weight:

$$P = (x_1, x_2)(w_{11}, w_{12}, w_{13})^T = (X_1, X_2, X_3) \tag{7}$$

Type, x_1 and x_2 for input layer saturation time and confining pressure.

- 3) Calculate the output of hidden layer:

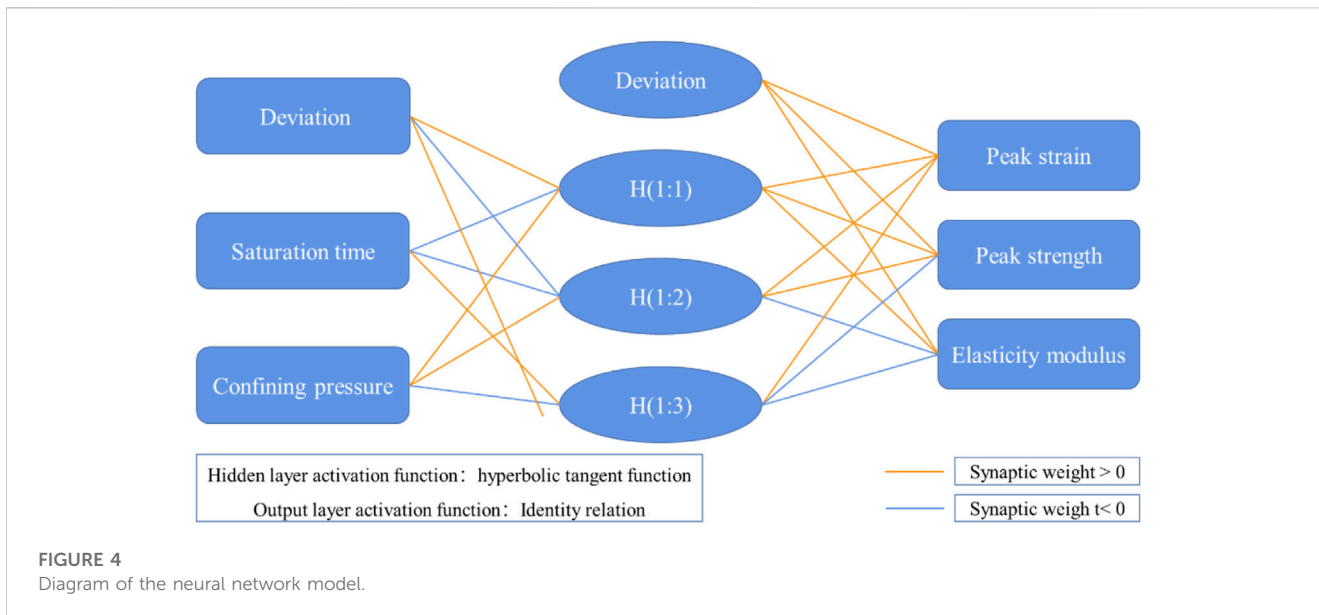


FIGURE 4 Diagram of the neural network model.

$$Y_1 = H(1: 1) = \tanh(X_1 + X_2 + X_3) \tag{8}$$

4) The error between the hidden layer output result and the real result was calculated:

$$\begin{cases} E = \frac{1}{2}(Y_{target} - Y_{out1})^2 \\ y_{out1} = \frac{e^{y_{net1}} - e^{-y_{net1}}}{e^{y_{net1}} + e^{-y_{net1}}} \\ y_{net1} = X_1 + X_2 + X_3 \end{cases} \tag{9}$$

where, E for error, Y_{net1} is the input signal received by the hidden layer, namely, the weighting of each factor and the input layer. Y_{out1} is the output value of the activation function of hidden layers.

5) Update weight:

Taking the saturation time factor as an example, updating the weights after the error back propagation requires first calculating the partial derivative of ω_{11} with the overall error, namely, $\frac{\partial E}{\partial \omega_{11}}$ value. For the convenience of calculation, $\frac{\partial E}{\partial \omega_{11}}$ can be decomposed into:

$$\frac{\partial E}{\partial \omega_{11}} = \frac{\partial E}{\partial y_{out1}} \cdot \frac{\partial y_{out1}}{\partial y_{net1}} \cdot \frac{\partial y_{net1}}{\partial \omega_{11}} \tag{10}$$

According to Eq. 9, the values of each split term are calculated in turn, and it can be seen that:

$$\begin{cases} \frac{\partial E}{\partial y_{out1}} = Y_{out1} - Y_{target} \\ \frac{\partial y_{out1}}{\partial y_{net1}} = \frac{\partial \left[\frac{e^z - e^{-z}}{e^z + e^{-z}} \right]}{\partial z} \Bigg|_{z=y_{net1}} = \frac{\partial \left[\frac{\sinh(z)}{\cosh(z)} \right]}{\partial z} = 1 - \tanh^2(z) = 1 - \left(\frac{e^{y_{net1}} - e^{-y_{net1}}}{e^{y_{net1}} + e^{-y_{net1}}} \right)^2 \\ \frac{\partial y_{net1}}{\partial \omega_{11}} = \frac{\partial (\omega_{11}x_1 + \omega_{12}x_2)}{\partial \omega_{11}} = x_1 \end{cases} \tag{11}$$

Substituting Eq. 11 into Eq. 10:

$$\frac{\partial E}{\partial \omega_{11}} = (Y_{out1} - Y_{target}) \cdot \left[1 - \left(\frac{e^{y_{net1}} - e^{-y_{net1}}}{e^{y_{net1}} + e^{-y_{net1}}} \right)^2 \right] \cdot x_1 \tag{12}$$

Using the calculation results of Equation 12, the value of the saturation time ω_{11} was updated:

$$\omega'_{11} = \omega_{11} - \eta \cdot \frac{\partial E}{\partial \omega_{11}} \tag{13}$$

The comparison of the results calculated by the neural network model in the figure with the original data is shown in Figure 5.

Figure 5 shows that the peak strain and peak strength prediction results obtained by the neural network model of the multilayer perceptron are highly similar to the original restoration results, while the difference between the peak modulus prediction results and the original data is more obvious. In order to analyze the fitting degree of the model in detail, the residual coefficients and correlation coefficients of the prediction results of the three dependent variables need to be calculated. The remaining error was calculated as follows:

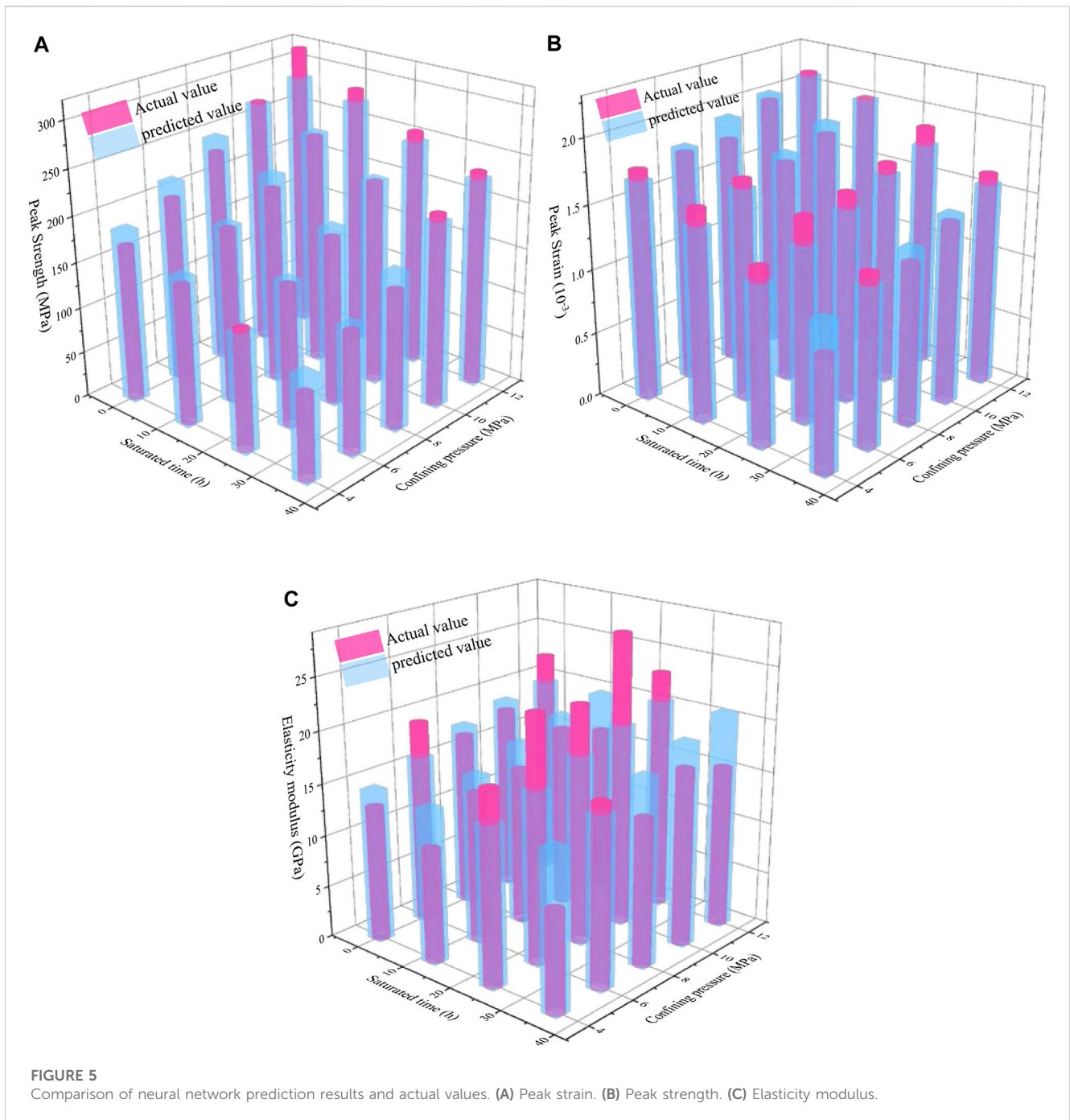
$$\delta_i = Y_i - y_i \tag{14}$$

$$\delta_i^* = \frac{\delta_i - \bar{\delta}}{\sigma} \tag{15}$$

where, δ_i is residual, Y_i is neural network forecast, Y_i is original value, δ_i^* is the standardization of residual value, $\bar{\delta}$ is the average of the residual, σ is the standard deviation. So, peak strain, peak strength and elastic modulus of the forecast curve and the correlation coefficient of the original curve R^2 can be calculated as follows:

$$R^2 = \frac{\sum_{i=1}^n \delta_i^2}{\sum_{i=1}^n (Y_i - \bar{y})^2} \tag{16}$$

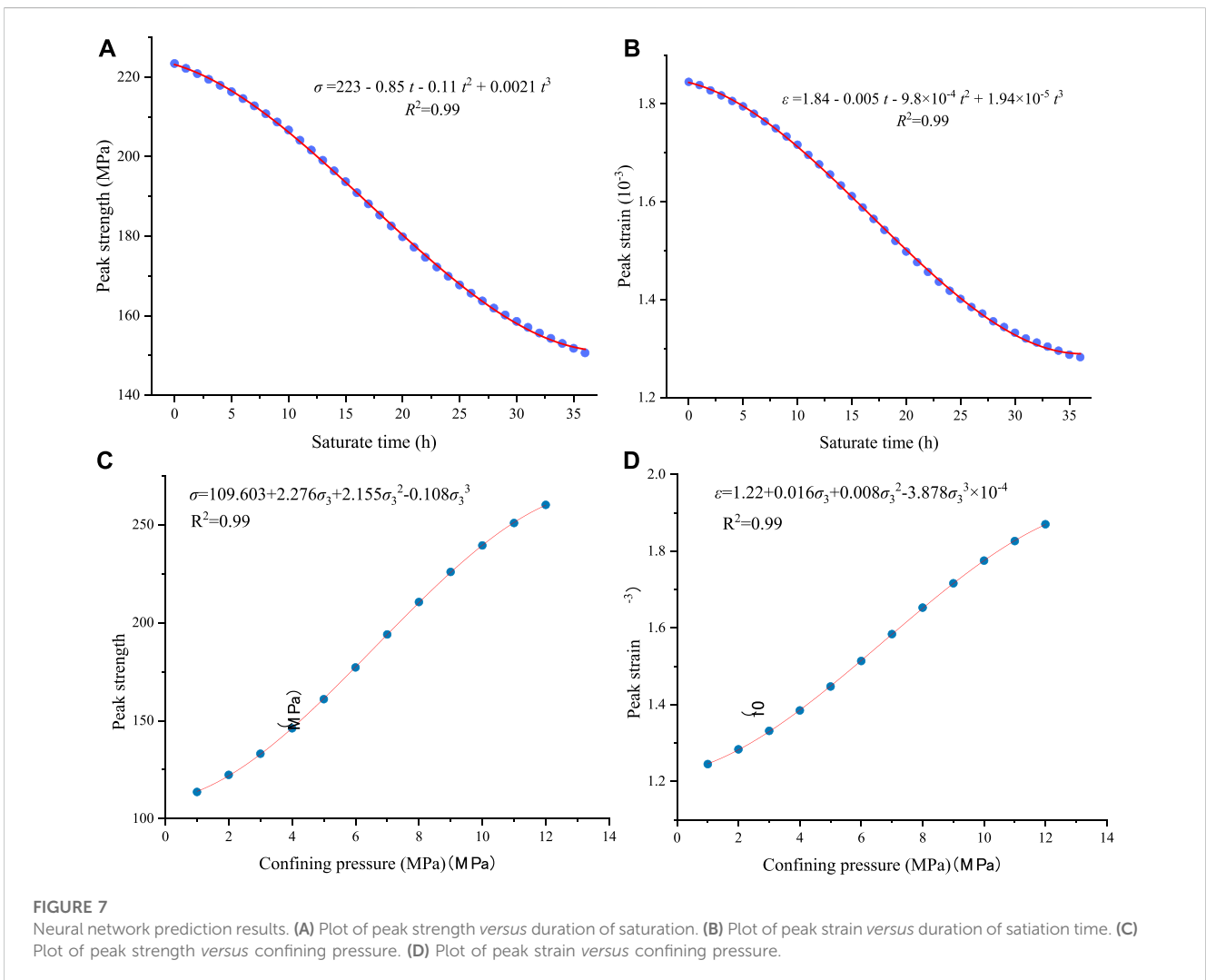
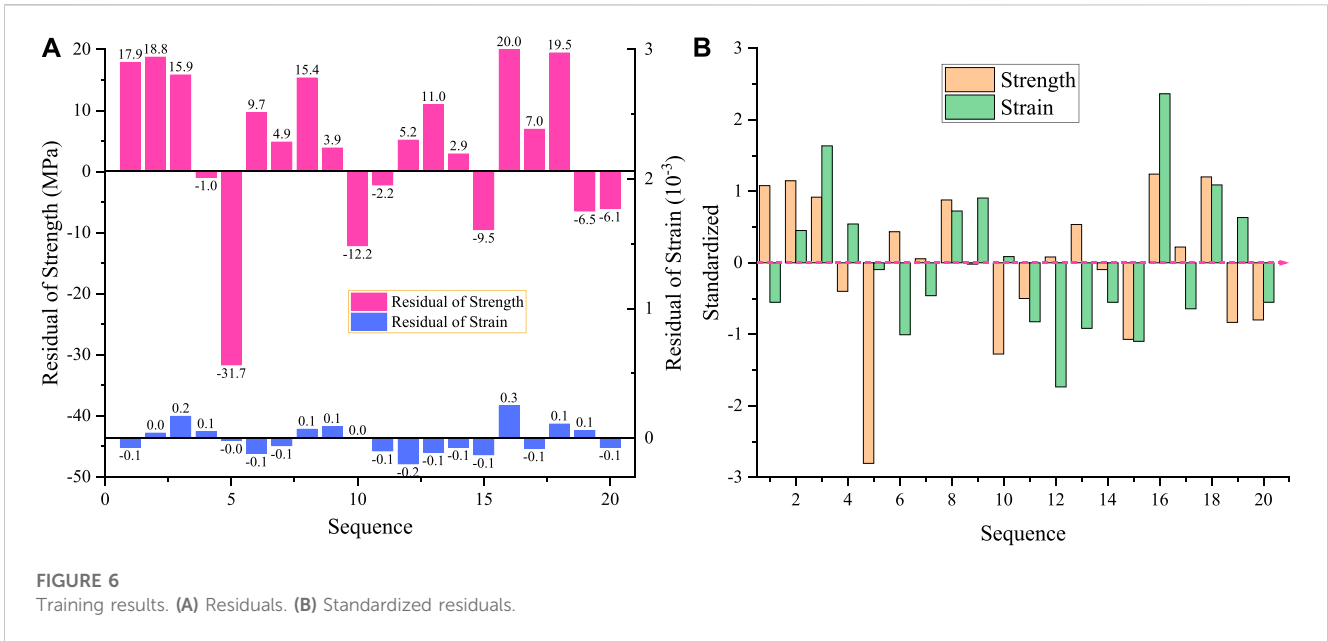
Figure 6 shows the residuals and standard deviations of the predicted peak strain and peak strength compared to the actual values. As can be seen from the figure, both standardized residual values are between [-2,2], The absolute value of the peak strain of



residual $|\delta_i|$ mostly falls in the interval $[0,20]$, the absolute value of the peak strength, residual $|\delta_i|$ mostly in the interval $[0,0.2]$. The correlation coefficient of peak strain was 0.93, the correlation coefficient of peak strength was 0.85. It is shown that the multi-layer perceptron neural network model has good results in the prediction of peak strain and peak strength. The correlation coefficient of elastic modulus was -2.98 . It shows that the multi-layer perceptron neural network model cannot predict the elastic modulus well, and further shows that the correlation between the input factor saturation time and the confining pressure and the elastic modulus is poor.

4.2 Neural network model prediction

The above calculation results show that the saturation time and confining pressure have little effect on the elastic modulus, so only the peak strain and peak strength are predicted in continuous intervals below. The discrete input factors of saturation time and confinement pressure were extended into a continuous domain and imported into the trained multi-layer perceptron neural network model for prediction, and 444 sets of predicted values were obtained. Among them, the saturation time was extended from 0, 12, 24, and 36 groups to a continuous



interval of 0–36, and the confining pressure was extended from 4, 6, 8, 10, and 12 groups to a continuous interval of 0–12.

Under the same saturation time, the average value of peak strain and peak strength corresponding to different confining pressures at the same saturation time was calculated, and 37 sets of data were obtained. Under the same confining pressure, the average value of peak strain and peak strength corresponding to different filling times under the same confining pressure was calculated to obtain 12 sets of data. The average value was calculated using the following formula:

$$\begin{cases} \sigma_n = \frac{1}{n} \sum_{i=1}^n x_i \\ \varepsilon_n = \frac{1}{n} \sum_{i=1}^n x_i \end{cases} \quad (17)$$

In the formula, σ_n is the average of peak strain, ε_n is the mean of the peak strength, x_i represents the corresponding peak stress and peak strength values for each group of variables, and n is the number of dependent variables.

To visualize the effects of saturation time and confining pressure on peak strain and peak strength, we fit the predicted curves separately. Different confining pressure values and different saturated time were used as independent variables, and peak strain and peak strength values were used as dependent variables. Cubic polynomials were used for fitting, and the fitting formula was as follows:

$$\begin{cases} \sigma = 223 - 0.85t - 0.11t^2 + 0.0021t^3 \\ \varepsilon = 1.84 - 0.005t - 9.8 \times 10^{-4}t^2 + 1.94 \times 10^{-5}t^3 \\ \sigma = 2.276\sigma_3 + 2.155\sigma_3^2 - 0.108\sigma_3^3 \\ \varepsilon = 0.016\sigma_3 + 0.008\sigma_3^2 - 3.878\sigma_3^3 \times 10^{-4} \end{cases} \quad (18)$$

The fitting curve is shown in Figure 7. The correlation between the fitted curve and the original data was 0.99, indicating that the cubic polynomial fitting effect was good, and the fitted curve could predict the peak strain and peak strength in a continuous interval. It can be seen from the figure that the peak strain and peak strength increase continuously with the increase of confining pressure, and the peak strain decreases gradually with the increase of water saturation time. Under the same water retention time, the peak strain and peak strength increased with the increase of confining pressure, and the increase amplitude showed a trend of first increasing and then decreasing. Under the same confining pressure, the peak strain and peak strength decreased with the increase of water saturation time, and the decreasing amplitude also showed a trend of first increasing and then decreasing.

5 Conclusion

In this paper, the degradation mechanism of phosphoric rock samples under different saturation duration was analyzed by laboratory test, theoretical analysis and neural network modeling, and the results is as follows:

- 1) The peak compressive strength and peak strain of the samples decreased gradually with the increase of saturation time. The average peak strength of 12, 24, and 36 h saturated specimens is 8.6%, 21.1%, and 32.2% lower than that of natural samples, and the peak strain is 5.9%, 13.9%, and 31.3% lower, respectively. It indicates that saturated water has obvious deterioration on mechanical properties of samples.
- 2) The stress-strain curves of the samples with water saturation for 36 h have more jitter stages after the peak, indicating that the plastic characteristics of the samples will be increased with water saturation for a long time.
- 3) The neural network model was established to characterize the change of mechanical properties of the samples. The average accuracy of the model was 0.89. This model can well show the variation of mechanical properties of samples under the action of saturated water and confining pressure.
- 4) The model can be used to predict and verify the mechanical properties of samples under other saturation and confining pressure conditions in the limited region. The research results can provide theoretical reference for the deterioration mechanism of confining pressure in water-rich roadway.

Data availability statement

The raw data supporting the conclusion of this article will be made available by the authors, without undue reservation.

Author contributions

CW supervised the research and proposed the research direction. SL was responsible for report analysis and paper writing. DZ, MW, FZ, and YP were responsible for data processing. All authors contributed to the article and approved the submitted version.

Conflict of interest

Authors SL, MW, and FZ were employed by Yunnan Phosphate Chemical Group Co., Ltd., Yunnan, China.

The remaining authors declare that the research was conducted in the absence of any commercial or financial relationships that could be construed as a potential conflict of interest.

Publisher's note

All claims expressed in this article are solely those of the authors and do not necessarily represent those of their affiliated organizations, or those of the publisher, the editors and the reviewers. Any product that may be evaluated in this article, or claim that may be made by its manufacturer, is not guaranteed or endorsed by the publisher.

References

- Aras, A., Ozsen, H., and Dursun, A. (2020). Using artificial neural networks for the prediction of bond work index from rock mechanics properties. *Mineral Process. Extr. Metallurgy Rev.* 41 (3), 145–152. doi:10.1080/08827508.2019.1575216
- Chen, C. (2021). *Experimental study on aging characteristics and deformation localization of rock under triaxial loading under water-rock coupling*. Chongqing, China: Chongqing University. doi:10.27670/dcnki.Gcqdu.2021.001103
- Chen, J., Chen, Z., and Pu, Y. (2022). Based on spectrum analysis and the convolution of the neural network of rock acoustic emission signal positioning study. *J. rock Mech. Eng.* 9 (S2), 3271–3281. doi:10.13722/j.carolcarrollnkijrme.2021.0836
- Chen, Q. (2022). *Rock mechanics parameters prediction experiments with drilling*. Beijing, China: China Mining University. doi:10.27623/dcnki.Gzkyu.2022.002321
- Feng, F., Chen, S., Wang, Q., Rostami, J., Khoreshok, A., Sheng, S., et al. (2022). Experimental study on failure characteristics of natural and saturated sandstone under true triaxial unloading and dynamic disturbance condition. *Chin. J. Rock Mech. Eng.* 41 (11), 2240–2253. doi:10.13722/j.cnki.jrme.2022.0040
- Feng, M. (2021). *Morphologic evolution and neural network prediction model of hydraulic fracture network in shale with natural fractures*. Chongqing, China: Chongqing university. doi:10.27670/dcnki.Gcqdu.2021.002399
- Jia, P., Wang, X., and Wang, D. (2023). Full water fracture rock deformation of freezing and thawing characteristic study. *Rock soil Mech.* 44 (02), 345–354. doi:10.16285/j.rsm.2022.0554
- Liu, S., and Li, X. (2023a). Experimental study on the effect of cold soaking with liquid nitrogen on the coal chemical and microstructural characteristics. *Sci. Pollut. Res.* 30 (3), 36080–36097. doi:10.1007/s11356-022-24821-9
- Liu, S., Sun, H., Zhang, D., Yang, K., Li, X., Wang, D., et al. (2023c). Experimental study of effect of liquid nitrogen cold soaking on coal pore structure and fractal characteristics. *Energy* 275 (7), 127470. doi:10.1016/j.energy.2023.127470
- Liu, S., Sun, H., Zhang, D., Yang, K., Wang, D., Li, X., et al. (2023b). Nuclear magnetic resonance study on the influence of liquid nitrogen cold soaking on the pore structure of different coals. *Phys. Fluids* 35 (1), 012009. doi:10.1063/5.0135290
- Ma, L., Huang, C., Meints, C., Morin, K. A., Dy, E., Tufa, K., et al. (2020). A full-scale case study on the leaching process of acid rock drainage in waste rock piles and the net infiltration through cover systems. *Water Air Soil Pollut.* 231 (6), 305. doi:10.1007/s11270-020-04660-5
- Moussas, V., and Diamantis, K. (2021). Predicting uniaxial compressive strength of serpentinites through physical, dynamic and mechanical properties using neural networks. *J. Rock Mech. Geotechnical Eng.* 13 (1), 167–175. doi:10.1016/j.jrmge.2020.10.001
- Ni, H., Wang, R., and Zhang, Y. (2005). Numerical simulation study on rock breaking mechanism and process under high pressure water jet. *Appl. Math. Mechanics-English Ed.* 26 (12), 1595–1604. doi:10.1007/BF03246268
- Shen, R., Li, T., Li, H., He, S., Zhao, E., Hou, Z., et al. (2021). Study on the effect of water on electromagnetic radiation characteristics of fractured sandstone under load. *Environ. Earth Sci.* 80 (3), 87. doi:10.1007/s12665-020-09338-z
- Wang, C., Liu, C., and Liu, D. (2019). Experimental study on volume effect of water-saturated fractured sandstone under uniaxial compression. *Chin. J. Undergr. Space Eng.* 15 (05), 1331–1340.
- Wang, C., Wei, S., Zhang, D., Yang, Y., Yu, B., and Pan, Y. (2023b). Physical properties and tensile strength evolution of gypsum materials under different water content conditions. *Constr. Build. Mater.* 364, 129865. doi:10.1016/j.conbuildmat.2022.129865
- Wang, C., Zhang, D., Yu, B., and Li, S. (2023a). Deformation and seepage characteristics of coal under true triaxial loading-unloading. *Rock Mech. Rock Eng.* 56, 2673–2695. doi:10.1007/s00603-022-03207-w
- Wang, F., Zhou, D., Zhou, X., Xiao, N., and Guo, C. (2020a). Rock breaking performance of TBM disc cutter assisted by high-pressure water jet. *Appl. Sciences-Basel* 10 (18), 6294. doi:10.3390/app10186294
- Wang, P., Yin, T., and Hu, B. (2020b). Dynamic tensile strength and failure mechanisms of thermally treated sandstone under dry and water-saturated conditions. *Trans. Nonferrous Metals Soc. China* 30 (8), 2217–2238. doi:10.1016/S1003-6326(20)65374-2
- Wei, S., Wang, C., Yang, Y., and Wang, M. (2020). Physical and mechanical properties of gypsum-like rock materials. *Adv. Civ. Eng.* 20, 1–17. doi:10.1155/2020/3703706
- Wood, J. (2015). Crushed-rock vs. full-diameter core samples for water-saturation determination in a tight-gas siltstone play. *Spe Reserv. Eval. Eng.* 18 (3), 407–416. doi:10.2118/174548-PA
- Wu, Y., Li, X., and Zhu, L. (2021). Fracture mechanism of rock collapse in the freeze-thaw zone of the eastern Sichuan-Tibet Mountains under seasonal fluctuating combinations of water and heat. *Nat. Hazards* 108 (2), 2309–2333. doi:10.1007/s11069-021-04781-y
- Zhang, Q., Song, J., and Nie, X. (1991). Application of neural network models to rock mechanics and rock engineering. *Int. J. Rock Mech. Min. Sci.* 28 (6), 535–540. doi:10.1016/0148-9062(91)91130-J
- Zhang, Q., Wang, J., Hou, L., and Lin, P. (2018). Study on the instability mechanisms and monitoring control of stratified rock slope with water-rich strata. *Geotechnical Geol. Eng.* 36 (3), 1665–1672. doi:10.1007/s10706-017-0421-7
- Zhao, L. (2022). Experimental study on mechanical property softening of saturated sandstone. *Chin. J. Undergr. Space Eng.* 18 (01), 154–162.